

BUDA-MESMERISE

Citation for published version (APA):

So, S., Park, H. W., Kim, B., Fritz, F. J., Poser, B. A., Roebroek, A., & Bilgic, B. (2022). BUDA-MESMERISE: Rapid acquisition and unsupervised parameter estimation for T-1, T-2, M-0, B-0, and B-1 maps. *Magnetic Resonance in Medicine*, 88(1), 292-308. <https://doi.org/10.1002/mrm.29228>

Document status and date:

Published: 01/07/2022

DOI:

[10.1002/mrm.29228](https://doi.org/10.1002/mrm.29228)

Document Version:

Publisher's PDF, also known as Version of record

Document license:

Taverne

Please check the document version of this publication:

- A submitted manuscript is the version of the article upon submission and before peer-review. There can be important differences between the submitted version and the official published version of record. People interested in the research are advised to contact the author for the final version of the publication, or visit the DOI to the publisher's website.
- The final author version and the galley proof are versions of the publication after peer review.
- The final published version features the final layout of the paper including the volume, issue and page numbers.

[Link to publication](#)

General rights

Copyright and moral rights for the publications made accessible in the public portal are retained by the authors and/or other copyright owners and it is a condition of accessing publications that users recognise and abide by the legal requirements associated with these rights.

- Users may download and print one copy of any publication from the public portal for the purpose of private study or research.
- You may not further distribute the material or use it for any profit-making activity or commercial gain
- You may freely distribute the URL identifying the publication in the public portal.

If the publication is distributed under the terms of Article 25fa of the Dutch Copyright Act, indicated by the "Taverne" license above, please follow below link for the End User Agreement:

www.umlib.nl/taverne-license

Take down policy

If you believe that this document breaches copyright please contact us at:

repository@maastrichtuniversity.nl

providing details and we will investigate your claim.

RESEARCH ARTICLE

Magnetic Resonance in Medicine

BUDA-MESMERISE: Rapid acquisition and unsupervised parameter estimation for T_1 , T_2 , M_0 , B_0 , and B_1 maps

Seohee So¹ | Hyun Wook Park¹  | Byungjai Kim¹ | Francisco J. Fritz² |
Benedikt A. Poser³  | Alard Roebroek³ | Berkin Bilgic^{4,5,6} 

¹School of Electrical Engineering, Korea Advanced Institute of Science and Technology (KAIST), Daejeon, Republic of Korea

²Institute of Systems Neuroscience, Center for Experimental Medicine, University Medical Center Hamburg-Eppendorf (UKE), Hamburg, Germany

³Department of Cognitive Neuroscience, Faculty of Psychology and Neuroscience, Maastricht University, Maastricht, The Netherlands

⁴Athinoula A. Martinos Center for Biomedical Imaging, Massachusetts General Hospital, Charlestown, Massachusetts, USA

⁵Department of Radiology, Harvard Medical School, Charlestown, Massachusetts, USA

⁶Harvard-MIT Health Sciences and Technology, Massachusetts Institute of Technology, Cambridge, Massachusetts, USA

Correspondence

Hyun Wook Park, School of Electrical Engineering, KAIST, 291 Daehak-ro, Yuseong-gu, Daejeon 34141, Republic of Korea.

Email: hwpark@kaist.ac.kr

Funding information

Bundesministerium für Bildung und Forschung, Grant/Award Numbers: 01EW1711A, 01EW1711B; Deutsche Forschungsgemeinschaft, Grant/Award Numbers: MO 2249/3-1, MO 2397/4-1, MO 2397/5-1; Dutch Science Foundation (NWO), Grant/Award Numbers: 016-178-052, 14637; European Research Council (ERC), Grant/Award Numbers: 639938, 885876; Forschungszentrums

Purpose: Rapid acquisition scheme and parameter estimation method are proposed to acquire distortion-free spin- and stimulated-echo signals and combine the signals with a physics-driven unsupervised network to estimate T_1 , T_2 , and proton density (M_0) parameter maps, along with B_0 and B_1 information from the acquired signals.

Theory and Methods: An imaging sequence with three 90° RF pulses is utilized to acquire spin- and stimulated-echo signals. We utilize blip-up/-down acquisition to eliminate geometric distortion incurred by the effects of B_0 inhomogeneity on rapid EPI acquisitions. For multislice imaging, echo-shifting is applied to utilize dead time between the second and third RF pulses to encode information from additional slice positions. To estimate parameter maps from the spin- and stimulated-echo signals with high fidelity, 2 estimation methods, analytic fitting and a novel unsupervised deep neural network method, are developed.

Results: The proposed acquisition provided distortion-free T_1 , T_2 , relative proton density (M_0), B_0 , and B_1 maps with high fidelity both in phantom and in vivo brain experiments. From the rapidly acquired spin- and stimulated-echo signals, analytic fitting and the network-based method were able to estimate T_1 , T_2 , M_0 , B_0 , and B_1 maps with high accuracy. Network estimates demonstrated noise robustness owing to the fact that the convolutional layers take information into account from spatially adjacent voxels.

Conclusion: The proposed acquisition/reconstruction technique enabled whole-brain acquisition of coregistered, distortion-free, T_1 , T_2 , M_0 , B_0 , and B_1 maps at $1 \times 1 \times 5 \text{ mm}^3$ resolution in 50 s. The proposed unsupervised neural network provided noise-robust parameter estimates from this rapid acquisition.

KEYWORDS

distortion correction, multicontrast MRI, quantitative MRI, stimulated echo, unsupervised parameter estimation

Medizintechnik Hamburg (FMTHH), Grant/Award Number: 01fmthh2017; Korea Institute of Science and Technology, Grant/Award Number: 2E30971; Korea Medical Device Development Fund, Grant/Award Number: 202011B35; MIT-Korea - KAIST Seed Fund of the MIT International Science and Technology Initiatives (MISTI); Federal Ministry of Education and Research; Research Foundation; European Research Council; National Institutes of Health, Grant/Award Numbers: P41-EB030006, R01-EB028797, R01MH111444, R03-EB031175, U01-EB025162, U01-EB026996; Ministry of Health; Korea Health Industry Development Institute, Grant/Award Number: HI14C1135

1 | INTRODUCTION

In MRI, signal intensity can be formulated in terms of biophysical parameters, such as longitudinal T_1 relaxation, transverse T_2 relaxation, and proton density (PD); and imaging parameters such as TE, TR, and flip angle (FA). Quantification of the biophysical parameters from acquired signals enables advanced characterization of the tissue, which improves clinical diagnosis and informs longitudinal studies.^{1–16}

Estimation of these biophysical parameters typically requires multiple measurements with various scan settings such as TI, TE, TR, and FA.^{17–20} The excessive imaging time required to make multiple acquisitions hampers the clinical application and translation of quantitative imaging. Whereas vulnerable patient populations (pediatric, elderly, acutely ill) may fail to comply with long imaging times, such lengthy acquisitions also increase the vulnerability to subject motion, resulting in potential estimation errors and misregistration between the estimated parameters.

There have been efforts toward rapidly estimating 1 or more MR parameters with single-type acquisition. Multiple spin-echo techniques^{21,22} acquire multiple spin echoes with different TE within a single TR by applying several refocusing pulses, which help shorten imaging time for T_2 estimation. However, these T_2 values may suffer from overestimation due to the stimulated and indirect echo present in the later echoes. T_2 estimation with multiple spin-echo signals, except the first echo signal, could mitigate the overestimation but still the overestimation appears. Bloch simulation-based echo-modulation curve fitting improves estimation accuracy, but it leads to a significant increase in the computation time. Double-echo

steady state (DESS)²³ estimates a T_2 map using simultaneously acquired steady-state free precession (SSFP)-FID and echo signals. There is a tradeoff between estimation accuracy and SNR of the acquired signal with respect to FA, and additional higher-order SSFP-FID acquisition is required to eliminate the tradeoff.²⁴ Optimized diffusion-weighted DESS with Cramér–Rao lower bound²⁵ has enabled simultaneous mapping of PD, T_1 , T_2 , and diffusion coefficient. These nonbalanced SSFP-based methods are highly sensitive to physiological motion disrupting the steady state. Inversion recovery TrueFISP²⁶ extracts T_1 , T_2 , and PD from the signal time course sampled with a series of balanced SSFP images after spin inversion. MR fingerprinting²⁷ collects the data by varying acquisition parameters such as FA, TR, TE, and sampling patterns in a pseudorandom manner. The estimation of the multiple tissue parameter is achieved through pattern recognition. MR spin tomography in time domain (MR-STAT)²⁸ employs a coupled space–time model formulating relationship between the time-varying signal and the physics of the experiment. It unifies the image reconstruction and parameter estimation into 1 process. Quantification of relaxation times and proton density by twin-echo saturation-recovery turbo-field echo (QRAPTEST)²⁹ determines T_1 , T_2 , PD, and B_1 field inhomogeneity using a single sequence in which each excitation is followed by 2 separate echoes. Quantitative imaging using configuration states (QuICS)³⁰ utilizes several SSFP images with varying RF spoiling, FA, and spoiling gradients for estimating T_1 , T_2 , and PD, as well as diffusion coefficient and B_1 field inhomogeneity.

Single-shot double-echo EPI³¹ acquires spin- and stimulated-echoes and proposes to manipulate T_1 and T_2

contrast using 3 RF pulses. Single-shot spin- and stimulated EPI (ss-SESTEPI)³² utilizes the T_1 manipulation property of this 3-pulse sequence for T_1 estimation. A limitation of the single-shot spin- and stimulated EPI method is that T_1 estimation accuracy depended on the mixing time (TM), the time interval between the second and the third RF pulses, and potential errors in B_1 correction from a minimum TM prescan can propagate into the T_1 estimate. Stimulated echo-based mapping (STEM)³³ performs estimation of T_1 , T_2 , and diffusion coefficient from stimulated echo signals and uses a protocol optimized with respect to the Cramér–Rao lower bound. In STEM, all parameters were entangled in 1 stimulated echo signal. Long TM optimized to create sufficient T_1 decay resulted in longer imaging time. Multiplexed echo-shifted multiband excited and recalled imaging STEAM encoded diffusion (MESMERISED)³⁴ acquired spin- and stimulated-echo signals from a 3-pulse STEAM sequence and introduced echo-shifting for efficient acquisition. MESMERISED estimated diffusion coefficient, T_1 , T_2 , and B_1 by changing b value, TM, TE, and FA, respectively, and showed more efficient and higher precision T_1 estimation from stimulated-echo/spin-echo ratio images compared to stimulated-echo images only. In MESMERISED, each parameter map was obtained by independent acquisitions rather than simultaneously. In addition, single-shot spin- and stimulated EPI, STEM, and MESMERISED were based on EPI acquisition; hence, they suffered from geometric distortion.

For parameter estimation, the majority of the conventional methods extract the tissue parameters from the acquired signals using dictionary matching or optimization based on signal models.^{22,35,36} Along with the advent of deep learning for MRI research in image reconstruction, analysis, and processing, parameter estimation methods using the neural networks have been proposed for fast and accurate relaxometry.^{37–41} The supervised learning method requires a large amount of training data. However, it may be difficult to obtain high-quality training data, including ground truth in the clinical field. If the training data are simulated, disagreement between the actual data and the simulated training data might be problematic.

In this study, the imaging sequence with three 90° RF pulses is utilized to rapidly acquire spin- and stimulated-echo signals for MR parameter estimation of T_1 , T_2 , M_0 , and B_1 . We change TE and TM together so that the signal is a function of both T_1 and T_2 relaxations. Single-shot EPI is used for rapid data acquisition. Two opposite phase-encoding polarities are used for estimating B_0 field inhomogeneity and eliminating geometric distortion, which hinders EPI from being used for quantitative MRI. We incorporate the echo-shifting approach proposed in MESMERISED to ensure high sampling

efficiency. Because we do not employ diffusion encoding in this work, we refer to this acquisition approach as blip-up/-down acquisition (BUDA)-MESMERISE. In addition, 2 parameter estimation methods, such as analytic fitting and unsupervised parameter estimation with a deep neural network, are performed to robustly estimate the MR parameters.

2 | THEORY

2.1 | Signal model

The proposed mapping of T_1 , T_2 , PD, and B_1 inhomogeneity is based on spin- and stimulated-echo signals acquired in quick succession. The imaging sequence with three 90° RF pulses is used for spin- and stimulated-echo acquisition, as shown in Figure 1A. The first RF pulse flips magnetization to the transverse plane. Before the second RF pulse, the transverse magnetization experiences T_2 decay and free precession. The second 90° pulse rotates the dephased magnetization around the B_1 field direction. This leads to partial refocusing of magnetization, and the amplitude of the partial spin echo becomes half of the magnetization that was tipped into the transverse plane by the first pulse. A subpopulation is converted to longitudinal magnetization after the second RF pulse. The longitudinal magnetization is converted back to transverse magnetization after the third RF pulse. This subpopulation is refocused following the third pulse after a time equal to the period between the first and the second RF pulses, that is, half of the TE.

In the proposed method, the spin-echo signal is acquired after the second RF pulse, and the stimulated-echo signal is acquired after the third RF pulse. To encode the spin- and stimulated-echoes, single-shot EPI is used for rapid acquisition and simplification of signal models. The acquired spin- and stimulated-echo signals are formulated as follows:

$$S_{SE} = M_0 \cdot \sin\left(\alpha_{B_1} \cdot \frac{\pi}{2}\right) \cdot \sin^2\left(\alpha_{B_1} \cdot \frac{\pi}{4}\right) \cdot e^{-\frac{TE}{T_2}} \quad (1)$$

$$S_{STE} = \frac{1}{2} \cdot M_0 \cdot \sin^3\left(\alpha_{B_1} \cdot \frac{\pi}{2}\right) \cdot e^{-\frac{TM}{T_1}} \cdot e^{-\frac{TE}{T_2}}, \quad (2)$$

where TM is the period between the second and the third RF pulses, and α_{B_1} represents the ratio between actual FA and nominal FA of 90°.

In order to estimate the tissue parameters, multiple acquisitions are made while changing the values of TE and TM. As the TM increases, the remaining time in TR for M_z recovery decreases. Therefore, signal intensity, except for the first acquisition, is affected by effective TR in the proposed imaging sequence as follows:

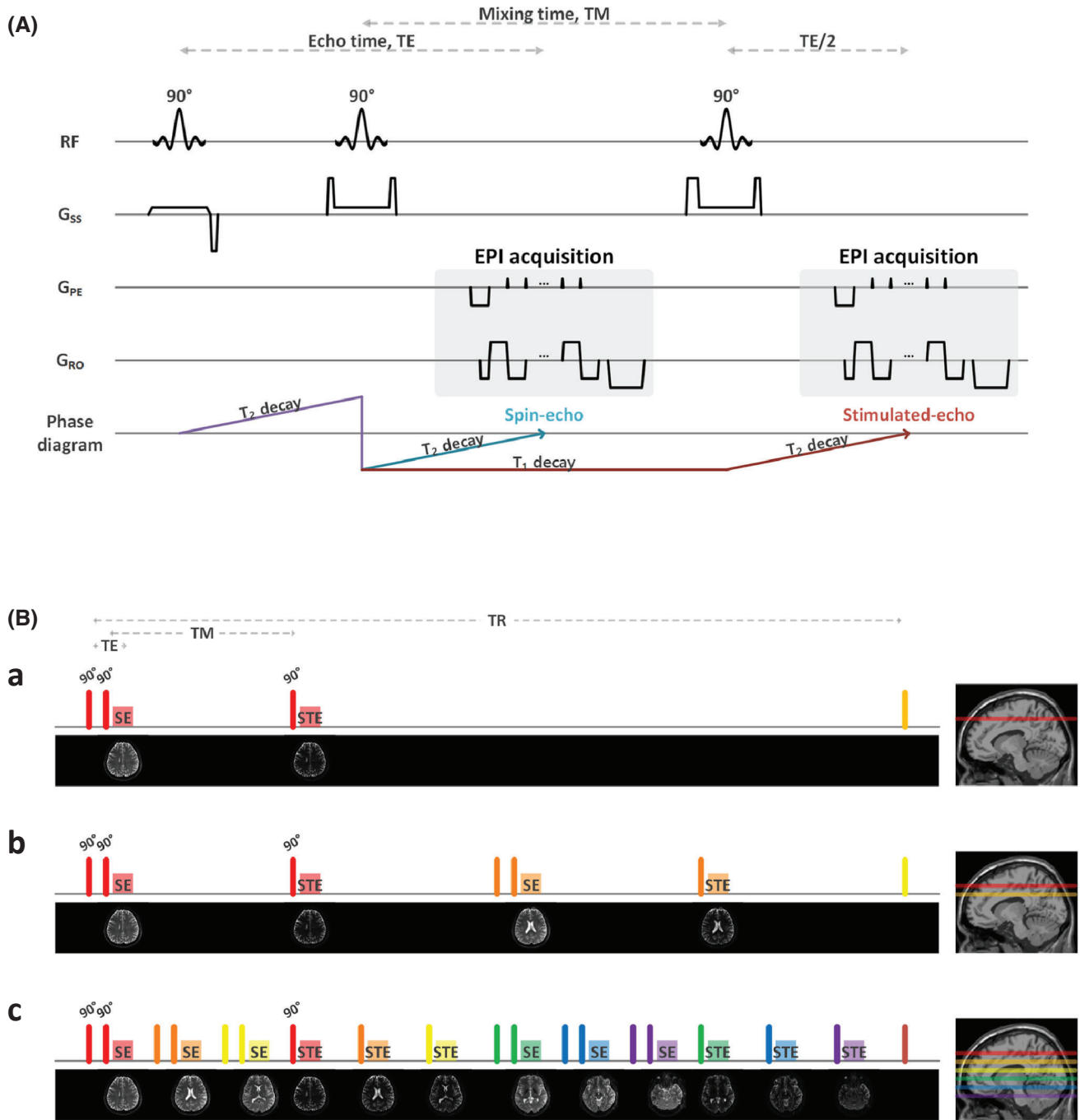


FIGURE 1 (A) The pulse sequence and phase diagram of the proposed method. Both spin echo and stimulated echo are acquired using an EPI readout. (B) Sequence diagrams without interleaving or echo-shifting (a), with interleaving (b), and with interleaving and echo-shifting (c). Number of slices acquired in 1 TR are 1 (a), 2 (b), and 6 (c), respectively

$$TR_{\text{eff}} = TR - \frac{TE}{2} - TM. \quad (3)$$

Accordingly, the acquired signal is represented as follows:

$$S_{\text{SE}} = M_0 \cdot \left(1 - e^{-\frac{TR_{\text{eff}}}{T_1}}\right) \cdot \sin\left(\alpha_{B_1} \cdot \frac{\pi}{2}\right) \cdot \sin^2\left(\alpha_{B_1} \cdot \frac{\pi}{4}\right) \cdot e^{-\frac{TE}{T_2}} \quad (4)$$

$$S_{\text{STE}} = \frac{1}{2} \cdot M_0 \cdot \left(1 - e^{-\frac{TR_{\text{eff}}}{T_1}}\right) \cdot \sin^3\left(\alpha_{B_1} \cdot \frac{\pi}{2}\right) \cdot e^{-\frac{TM}{T_1}} \cdot e^{-\frac{TE}{T_2}}. \quad (5)$$

The detailed signal formation and effective longitudinal recovery for the following acquisition are derived in Supporting Information.

2.2 | Blip-up/blip-down acquisition (BUDA)

In EPI, the presence of local magnetic field inhomogeneity leads geometric distortion. In order to eliminate these distortions, we adopt BUDA.^{42,43} BUDA acquires 2 shots of EPI with opposite phase-encoding directions. When the direction of the phase encoding is reversed, geometric distortion occurs in the opposite direction, as shown in Figure 2. With 2 opposite-polarity images, B_0 field inhomogeneity map can be estimated using techniques such as FSL topup.^{44,45} Acquired k-space data of each shot is first processed individually with POCSENSE,⁴⁶ and then ΔB_0 estimation is carried out using the reconstructed images. BUDA reconstruction incorporates the estimated field inhomogeneity into the parallel imaging forward model and employs a Hankel structured low-rank constraint.^{47–50} The forward model represents data consistency that the acquired data should match the distorted data synthesized with the estimated field inhomogeneity and the distortion-free image to be estimated. The Hankel structured low-rank constraint exploits similarities between the opposite-polarity images while mitigating potential shot-to-shot phase variations. The BUDA reconstruction is represented as follows:

$$\min_{\mathbf{I}_u, \mathbf{I}_d} \|\mathbf{F}_u \mathbf{E}_u \mathbf{C} \mathbf{I}_u - \mathbf{k}_u\|_2^2 + \|\mathbf{F}_d \mathbf{E}_d \mathbf{C} \mathbf{I}_d - \mathbf{k}_d\|_2^2 \quad (6)$$

subject to $\text{rank}(\mathcal{H}(\mathbf{I})) = r$,

where \mathbf{F}_u and \mathbf{F}_d are the Fourier operators for under-sampled blip-up and blip-down acquisitions, respectively; \mathbf{E}_u and \mathbf{E}_d are the geometric distortion operators due to field inhomogeneity in blip-up and blip-down acquisitions, respectively; \mathbf{C} are the coil sensitivities estimated from distortion-free gradient-echo calibration data using ESPIRiT⁵¹; \mathbf{I}_u and \mathbf{I}_d are the distortion-free images; \mathbf{k}_u and \mathbf{k}_d are k-space data for blip-up and blip-down acquisitions, respectively; \mathbf{I} is the set of distortion-free images, $\begin{bmatrix} \mathbf{I}_u \\ \mathbf{I}_d \end{bmatrix}$; $\mathcal{H}(\cdot)$ is the block-Hankel representation; and $\|\cdot\|_2$ is l_2 norm operator. 5×5 block is used for the block-Hankel representation. The block-Hankel representation is implemented by consecutively selecting 5×5 neighboring points in k-space data of each shot and then concatenating them in the column dimension. Λ is regularization parameter, $r = \lfloor 1.25 \times (\text{number of block elements}) \rfloor = 31$ in our experiment.

2.3 | Echo-shifting acquisition

Whereas using a larger TM increases T_1 sensitivity, it also increases the dead time between the second and

the third RF pulses, which reduces the acquisition efficiency. We incorporate the MESMERISED echo-shifting approach³⁴ to ensure high acquisition efficiency. During the dead time, data acquisition of different slice starts as shown in Figure 1B. Concerning the stimulated echo of the first slice, the magnetization that would form the stimulated echo is stored as longitudinal magnetization after the second RF pulse. The longitudinal magnetization is not affected by RF pulse of the different slice and gradient field. Therefore, echo-shifting acquisition can be performed during the dead time without interference between different slices,³⁴ as also shown in Results. We refer to the number of the echo-shifted slices as the echo-shift factor, as in MESMERISED, although it is technically different from standard echo-shifting approaches, which achieve $TE > TR$.^{52,53} Because the proposed sequence is composed of 90° pulses and does not utilize high-energy 180° inversion or refocusing pulses, specific absorption rate (SAR) and RF amplitude are relatively benign compared with inversion recovery-prepared sequence for T_1 estimation and spin-echo- or turbo-spin-echo-based sequence for T_2 estimation. For this reason, the SAR burden of the proposed method is comparatively low even when densely packed acquisition and multiband excitation are used. Accordingly, high multiplicative (echo-shift factor) \times (multiband acceleration factor) can be achieved.

2.4 | Parameter estimation

The spin-echo signal is formulated by M_0 , α_{B1} , and exponential decay of T_2 modulated by TE in Equation (1); and stimulated-echo signal is affected by M_0 , α_{B1} , exponential decay of T_2 modulated by TE, and exponential decay of T_1 modulated by TM in Equation (5). We introduce 2 methods for estimating T_1 , T_2 , M_0 , and α_{B1} . The first approach is an analytic method with dictionary matching, whereas the second approach uses unsupervised neural network-based optimization.

2.4.1 | Analytic fitting

In the signal ratio between stimulated echo and spin echo, T_2 decay effect and PD component are eliminated. The ratio follows simple exponential T_1 decay with respect to TM, as follows:

$$\frac{S_{STE}}{S_{SE}} = \frac{1}{2} \cdot \left\{ \frac{\sin\left(\alpha_{B1} \cdot \frac{\pi}{2}\right)}{\sin\left(\alpha_{B1} \cdot \frac{\pi}{4}\right)} \right\}^2 \cdot e^{-\frac{TM}{T_1}}. \quad (7)$$

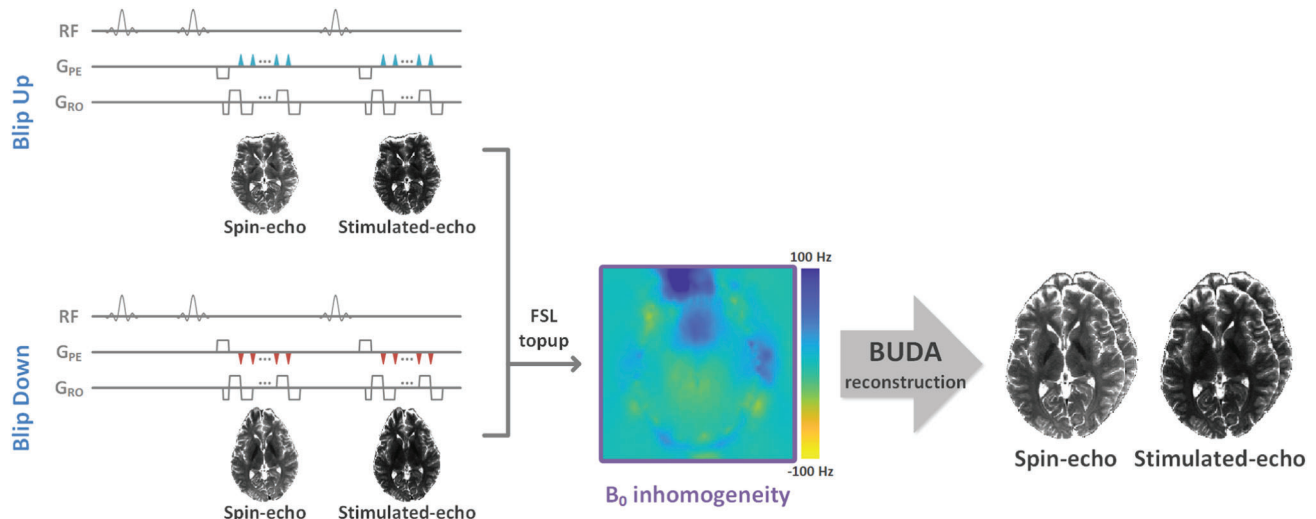


FIGURE 2 Schematic diagram of blip-up/down acquisition and reconstruction.

T_1 and α_{B1} are estimated from the above ratio. From the signal evolution with various TM values, T_1 and $\{S_{STE}/S_{SE}\}_{TM=0}$ can be estimated. The value of $\{S_{STE}/S_{SE}\}_{TM=0}$, which equals to $(1/2) \cdot \{\sin(\alpha_{B1} \cdot \pi/2) / \sin(\alpha_{B1} \cdot \pi/4)\}^2$, and α_{B1} have a monotonic relation when α_{B1} is in the range of $[0, 2]$, as shown in Figure 3. The monotonic relation enables us to determine α_{B1} from the estimate $\{S_{STE}/S_{SE}\}_{TM=0}$. The estimates are obtained by projection-based dictionary matching that is established based on the Bloch equation as follows:

$$\arg \max_{\mathbf{d}^{1 \times n} \in \mathbf{D}} \frac{\mathbf{d} \cdot \mathbf{S}}{\|\mathbf{d}\|_2} \quad (8)$$

$$\left\{ \frac{S_{STE}}{S_{SE}} \right\}_{TM=0} = \frac{\mathbf{d} \times \mathbf{S}^T}{\|\mathbf{d}\|_2^2}, \quad (9)$$

where \mathbf{d} denotes the signal vector of $1 \times n$ in dictionary; \mathbf{S} denotes the measured signal vector of $1 \times n$; n is the number of acquisitions; and \mathbf{D} is the dictionary of the signal vectors. With the prior knowledge that B_1 field is spatially smooth, estimated α_{B1} can be refined by polynomial fitting, and T_1 can be re-estimated using the polynomial fitted α_{B1} to improve the estimation performance.

The estimated T_1 and α_{B1} values are plugged in the spin- and stimulated-echo signal equation, which now only contains T_2 and M_0 unknowns and follows a simple exponential decay with respect to TE.

$$\begin{aligned} S'_{SE} &= S_{SE} / \left\{ \left(1 - e^{-\frac{TR_{eff}}{T_1}} \right) \cdot \sin \left(\alpha_{B1} \cdot \frac{\pi}{2} \right) \cdot \sin^2 \left(\alpha_{B1} \cdot \frac{\pi}{4} \right) \right\} \\ &= M_0 \cdot e^{-\frac{TE}{T_2}} \end{aligned} \quad (10)$$

$$\begin{aligned} S'_{STE} &= S_{STE} / \left\{ \frac{1}{2} \cdot \left(1 - e^{-\frac{TR_{eff}}{T_1}} \right) \cdot \sin^3 \left(\alpha_{B1} \cdot \frac{\pi}{2} \right) \cdot e^{-\frac{TM}{T_1}} \right\} \\ &= M_0 \cdot e^{-\frac{TE}{T_2}}. \end{aligned} \quad (11)$$

Two approaches can be considered to estimate T_2 and M_0 from the spin- and stimulated-echo signals. One is a simple $M_0 \cdot \exp(-TE/T_2)$ decay fitting with the compensated signals, S'_{SE} and S'_{STE} . The other way is to fit the S_{SE} and S_{STE} signal evolutions with the dictionary generated using the estimated T_1 and α_{B1} . We use the latter approach because it can avoid noise amplification caused by the division-based compensation. The overall process of the analytic-fitting method is shown in Figure 3.

2.4.2 | Unsupervised parameter estimation with deep neural network

In order to exploit spatial relations between neighboring voxels, we propose a convolutional neural network-based parameter estimation method. A residual network,⁵⁴ which is known to be easy to optimize, is utilized as the parameter estimation network, and its detailed structure is shown in Figure 4. In order to limit the parameter range, the sigmoid function is used as activation function of the last layer. Input to the parameter estimation network is a set of spin- and stimulated-echo images for various [TE, TM]s. The parameter estimation network produces T_1 , T_2 , and M_0 maps as its outputs. From the estimated T_1 , T_2 , and M_0 maps and the polynomial-fitted α_{B1} estimated from analytic fitting, spin- and stimulated-echo signals, S_{SEs} and S_{STEs} , are synthesized by a Bloch generator that is implemented by Equations (4) and (5). In addition, the

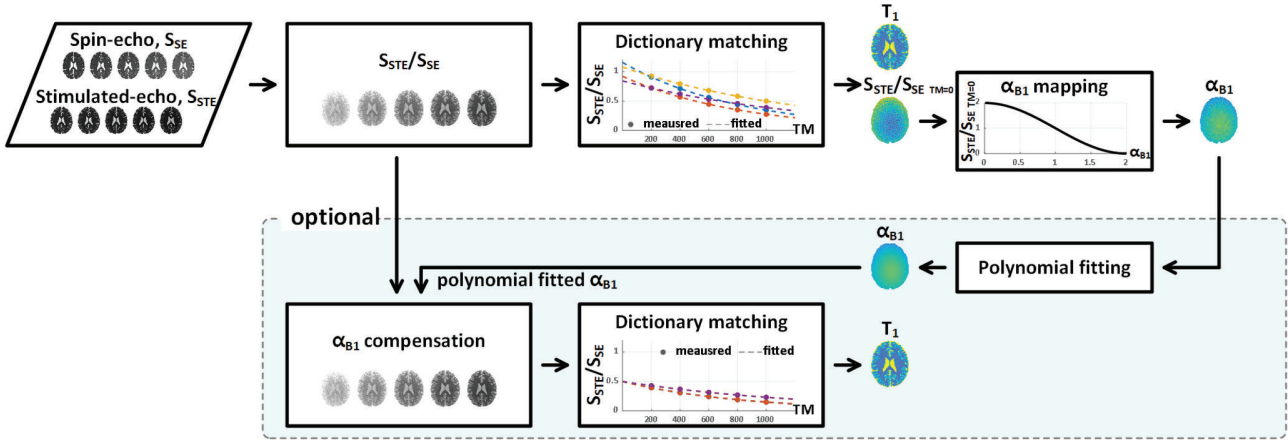
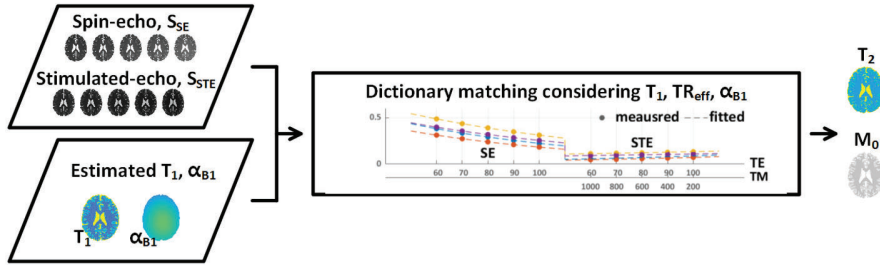
(A) Estimation of T_1 and α_{B1} (B) Estimation of T_2 and M_0 

FIGURE 3 Flow chart of the analytic-fitting method for parameter estimation

stimulated-echo signal can be obtained from the spin-echo signal by using Equation (7) as follows:

$$S'_{STEs} = \frac{1}{2} \cdot S_{SEm} \cdot \frac{\sin^2\left(\alpha_{B1} \cdot \frac{\pi}{2}\right)}{\sin^2\left(\alpha_{B1} \cdot \frac{\pi}{4}\right)} \cdot e^{-\frac{TM}{T_1}}. \quad (12)$$

The synthesized spin-echo signal, S_{SEs} from Equation (4), and 2 synthesized stimulated-echo signals, S_{STEs} from Equation (5) and $S_{STEs'}$ from Equation (12), are compared with the corresponding measured signals, S_{SEm} and S_{STEM} , to train the network. The differences between the input images and the synthesized images are utilized as a loss function of the network, thereby obviating the need for any additional ground truth information during training of the network weights, where the loss function is defined as follows:

$$\text{Loss} = \lambda_1 \cdot |S_{SEm} - S_{SEs}| + \lambda_2 \cdot |S_{STEM} - S_{STEs}| + \lambda_3 \cdot |S_{STEM} - S_{STEs'}|, \quad (13)$$

where λ_1 , λ_2 , and λ_3 are regularizing parameters and we use $\lambda_1 = \lambda_2 = \lambda_3 = 1$. The Adam optimizer⁵⁵ is used for

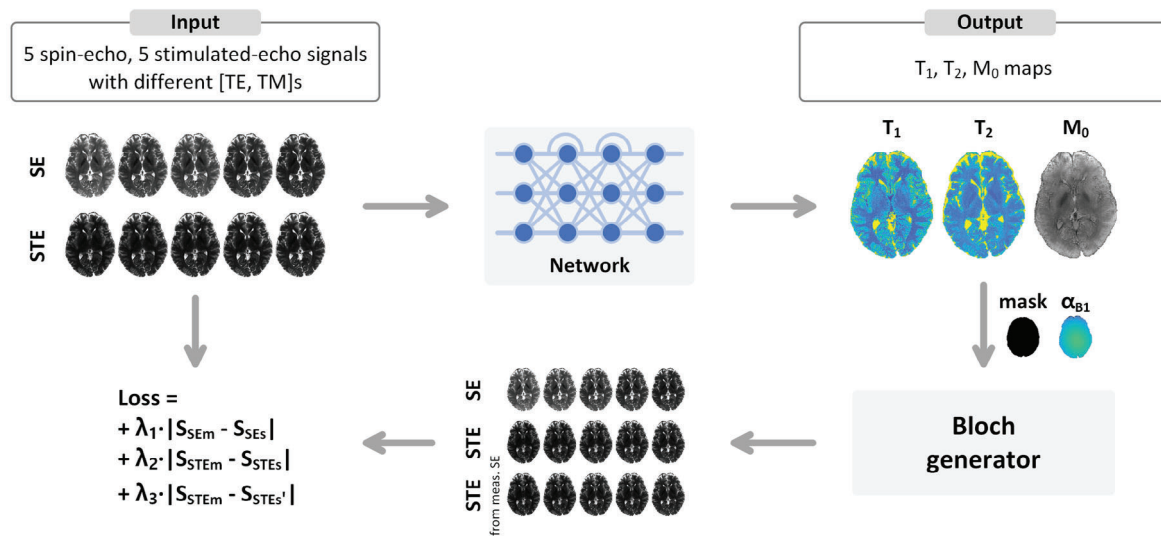
the optimization process. The proposed parameter estimation method is unsupervised in the sense that the network does not require ground truth parameter maps for training. Hence, this estimation method functions as more of an optimization method with a deep neural network than deep learning. The network provides noise robustness through convolution layers and enforces the synthesized maps to obey Bloch modeling through the loss function.

In order to validate the proposed unsupervised parameter estimation with a deep neural network, we designed a numerical phantom experiment. Supporting Information Figure S2 reveals that the proposed estimation method provides accurate estimate without ground truth.

3 | METHODS

Phantom and in vivo MRI experiments were conducted to validate the proposed method on a 3 Tesla MRI scanner (Magnetom Verio, Siemens, Germany). The proposed rapid spin- and stimulated-echo imaging was performed

(A) Unsupervised parameter estimation with deep neural network



(B) Network structure

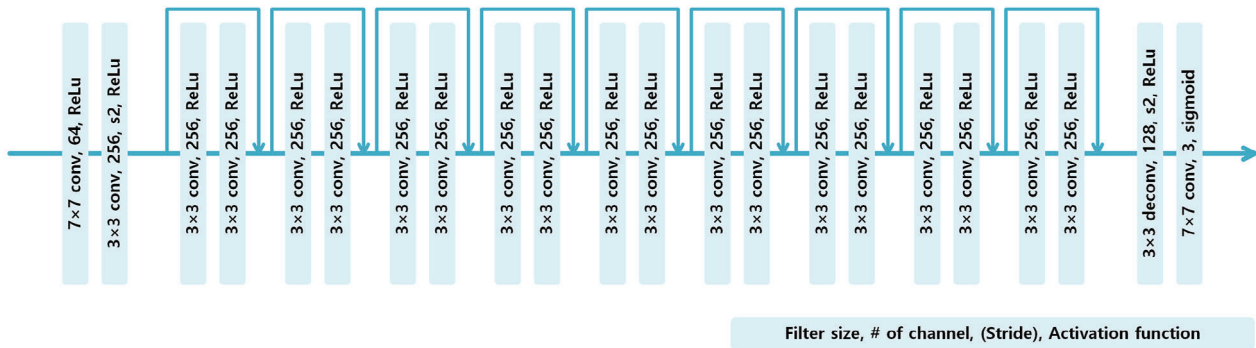


FIGURE 4 (A) Schematic diagram of the unsupervised parameter estimation with deep neural network. (B) Network structure used for the proposed parameter estimation method

with 5 combinations of [TE, TM]. For each [TE, TM] pair, 2 scans with opposite phase-encoding directions were conducted. In order to minimize fitting noise in T_1 estimation, we tried to make the SNR of the signal ratio between stimulated echo and spin echo less varying by decreasing TM as TE increased. For coil-sensitivity estimation, a gradient-echo image with short TR and short TE was acquired. T_1 , T_2 , M_0 , and α_{B1} maps were estimated from the 5 spin- and stimulated-echo images following the proposed parameter estimation methods. For reference information, inversion recovery (IR)–spin echo (SE) and IR–SE–EPI for T_1 and SE and SE–EPI for T_2 were applied, and the tissue parameters were estimated by using the projection-based dictionary matching of Equation (8).

3.1 | Phantom acquisition

A carrageenan, agarose, and $GdCl_3$ phantom⁵⁶ consisting of 12 vials with various T_1 and T_2 values was prepared. Detailed imaging parameters are presented in Table 1. For the neural network estimation, with initial learning rate of 4×10^{-5} and optimizer momentum of 0.9, 1000 epochs took about 167s for the estimation using GPU (Titan X, NVIDIA, United States). For quantitative analysis, a 12-mm radius region of interest was selected for each vial.

3.2 | In vivo acquisition

In vivo brain experiment was conducted with institutional review board approval.

TABLE 1 Imaging parameters for single-slice phantom experiments.

Sequence	FOV (mm)	Resolution (mm)	Slice (mm)	TR (s)	TE/TM/TI (ms)	BW (Hz/Px)	ESP (ms)	ETL	PF	R	RS
Proposed 25 s	224 × 224	1 × 1	5	2.5	[TE, TM] = [120, 150], [110, 400], [100, 600], [90, 800], [82, 1000]	830	1.31	84	6/8	2	○
IR-SE 2880 s	256 × 256	1 × 1	5	3	TE = 12 TI = 250, 500, 750, 1000, 1250	130	-	-	6/8	-	-
IR-SE-EPI 150 s	256 × 256	2 × 2	5	30	TE = 90 TI = 250, 500, 750, 1000, 1250	832	1.27	96	6/8	-	○
SE 2880 s	256 × 256	1 × 1	5	3	TE = 12, 25, 50, 75, 100	130	-	-	-	-	-
SE-EPI 150 s	256 × 256	2 × 2	5	30	TE = 90, 100, 110, 120, 130	832	1.27	96	6/8	-	○
GRE 1.28 s	256 × 256	2 × 2	5	0.01	TE = 4	260	-	-	-	-	-

GRE scan is the calibration scan for coil sensitivity estimation. Abbreviations: BW, bandwidth; ESP, echo spacing; ETL, echo train length; GRE, gradient echo; IR, inversion recovery; PF, partial Fourier; R, in-plane acceleration factor; RS, ramp sampling; SE, spin echo; TM, mixing time.

(I) *Single-slice acquisition*: Detailed imaging parameters are presented in Table 2. For the neural network estimation, an initial learning rate of 10^{-4} , optimizer momentum of 0.9, and 1000 epochs were used, which took about 167 s. Histogram analysis was used for quantitative comparison, thereby avoiding potential errors due to misregistration between the estimated parameter maps.

(II) *Whole-brain acquisition*: Twenty-four slices were acquired per TR. Echo-shifting acquisition, interleaved acquisition, and multiband acquisition were combined. The echo-shift and interleave factors were adjusted according to TE and TM while maintaining constant TR.³⁴ [TE, TM, echo-shift factor, interleave factor] = [120, 140, 1, 12], [110, 320, 2, 6], [100, 500, 3, 4], [90, 750, 4, 3], [82, 1000, 6, 2] were used, and multiband factor of 2 was utilized with blipped-CAIPIRINHA.⁵⁷ Twenty-four slices without slice gap were sampled with odd/even order slice-interleaving scheme, where data from every other slice is acquired and then that of omitted slices is obtained. The other experimental conditions were same as those of the single slice experiment. The effective TR changed according to the slice position due to varying echo-shift factor and interleave factor with single-shot EPI acquisition, as shown in Supporting Information Figure S4. The tissue parameters, T_1 , T_2 , M_0 , and α_{B1} , were estimated from the 5 spin-echo images and 5 stimulated-echo images in a slice-by-slice manner.

4 | RESULTS

4.1 | Phantom experiment

Acquired blip-up/-down and distortion-corrected phantom images are shown in Supporting Information Figure S5. The proposed reconstruction with BUDA successfully corrected geometric distortion in EPI. Signal intensity of the 5 stimulated-echo signals were similar because TE and TM changed in opposite ways in order to retain the SNR level. Supporting Information Figure S6 shows spin-echo images acquired by the proposed pulse sequence with TR = 30 s, where the signal intensity was not affected by spin history, and TR = 2.5 s case where the signal intensity was affected by the incomplete M_z recovery. Signal difference between the spin-echo images with TR = 30 s and TR = 2.5 s shows that the effective TR should be considered when T_2 relaxation time is estimated from the spin-echo data with a short TR.

Parameter estimation results from the proposed and conventional methods are shown in Figures 5 and 7. Qualitative and quantitative comparisons are presented in Figures 5 and 7A, respectively. In the results from EPI-based methods, IR-SE-EPI, SE-EPI, and STEM, geometric distortions were observed. On the contrary, geometric distortion were corrected with the proposed BUDA acquisition. The BUDA acquisition and reconstruction for

TABLE 2 Imaging parameters for in vivo experiments

Sequence	FOV (mm)	Resolution (mm)	Slice (mm)	TR (s)	TE/TM/TI (ms)	BW (Hz/Px)	ESP (ms)	ETL	PF	R	RS	FS
Proposed 50 s	224 × 224	1 × 1	5	5	[TE, M] = [120, 140], [110, 320], [100, 500], [90, 750], [82, 1000]	830	1.31	84	6/8	2	○	○
IR-SE 960 s	256 × 256	2 × 2	5	1.5	TE = 12 TI = 200, 400, 600, 800, 1000	130	-	-	-	-	-	-
IR-SE-EPI 100 s	224 × 224	2 × 2	5	20	TE = 44 TI = 200, 400, 600, 800, 1000	1654	0.68	84	6/8	-	○	○
SE 960 s	256 × 256	2 × 2	5	1.5	TE = 12, 40, 60, 80, 100	130	-	-	-	-	-	-
SE-EPI 100 s	224 × 224	2 × 2	5	20	TE = 44, 60, 75, 90, 105	1654	0.68	84	6/8	-	○	○
GRE 0.64 s	256 × 256	4 × 4	5	0.01	TE = 4	260	-	-	-	-	-	-

Abbreviation: FS, fat suppression.

the distortion correction could be also applied to the reference EPI-based methods. In terms of T_1 and T_2 values, the proposed and conventional methods show similar results even though BUDA-MESMERISE was faster with an imaging time of 25 s. For coil sensitivity measurement, the central 24 lines were taken from 1.28 s calibration gradient-echo scan. STEM parameter estimation was conducted for the stimulated-echo signal by least-square fitting. Considering that the scan parameters were not optimized as proposed in the original STEM approach,³³ results appeared to be noisier and less accurate. This was likely because both T_1 and T_2 were estimated from stimulated-echo signal with lower SNR. The proposed method used spin- and stimulated-echo signals to estimate T_1 and T_2 ; hence, it was possible to estimate the parameters more accurately. Figure 5C–E shows ΔB_0 maps estimated by FSL topup with the BUDA acquisition, α_{B1} map, and M_0 maps, respectively. The estimated results with the analytic fitting and the neural network were similar for all parameters. Network estimation gave less noisy parameters with smaller variation owing to the fact that the convolutional network took information of spatially adjacent voxels into account. By contrast, the conventional pixel-by-pixel fitting with dictionary matching showed relatively noisy estimates.

4.2 | In vivo experiment

Acquired blip-up/-down brain images and distortion-corrected image are shown in Supporting Information Figure S7. In the in vivo experiment, geometric

distortion was successfully eliminated by the BUDA acquisition and reconstruction. T_1 and T_2 estimation results from the proposed and conventional methods are shown in Figure 6. In the results from the EPI-based conventional method, geometric distortions were observed, which were corrected with BUDA-MESMERISE. Comparing the estimated parameter maps, both T_1 and T_2 from the proposed method agreed with the results of the conventional spin echo-based methods. The effect of the slice profile on the estimated parameters was investigated with numerical phantom simulation and presented in the Supporting Information Figure S8. When comparing the proposed analytic fitting and neural network estimation, the neural network estimates were less noisy than analytic fitting, which was particularly evident in the M_0 map. The comparison results of M_0 , ΔB_0 , and α_{B1} between the proposed and reference methods are presented in Supporting Information Figure S9. In addition, the loss of the neural network estimation according to the epoch and the parameter estimation results after 5 different epochs are shown in the Supporting information Figure S10.

We conducted a histogram comparison to avoid registration error between the parameter maps from different methods. Quantitative histogram analysis is presented in Figure 7B. Because the resolutions of the proposed and conventional methods are different, the histograms were normalized by the total number of voxels in the same FOV. A T_1 peak around 650 ms observed in T_1 histogram of IR-SE was not shown in those of IR-SE-EPI and the proposed method. The T_1 peak of IR-SE was presumed due to the presence of the lipid component from

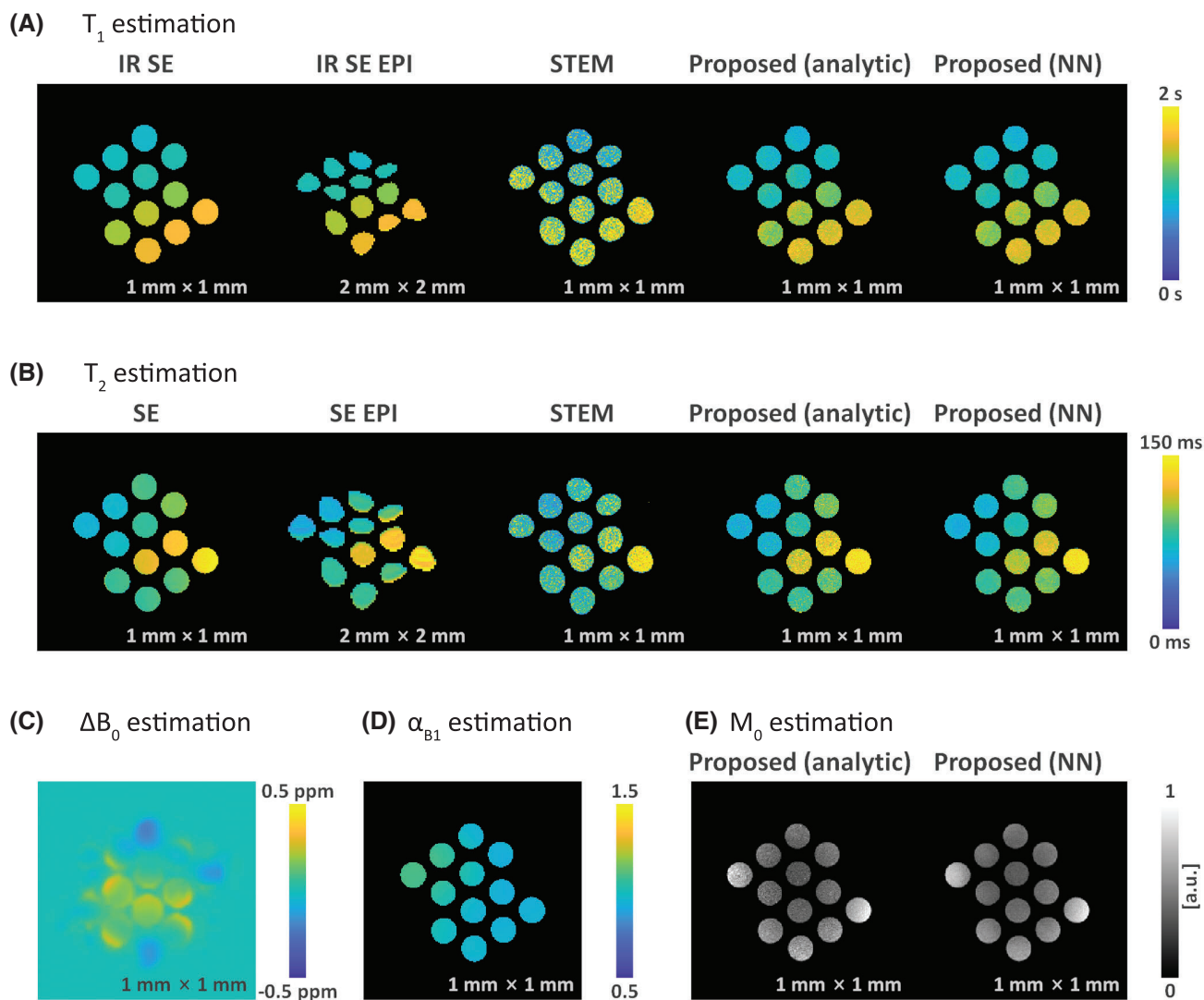


FIGURE 5 Phantom experiment results. Qualitative comparison of the proposed method with conventional methods. (A) T_1 estimation results. (B) T_2 estimation results. (C–E) ΔB_0 , α_{B1} , and M_0 estimation results from the proposed method, respectively

myelin,⁵⁸ which was not suppressed, whereas the fat suppression was applied for the IR-SE-EPI and the proposed method. Both T_1 and T_2 estimates have similar parameter distributions to the conventional methods; however, using the proposed method, the parameter distribution was more widely spread. This broadening in the distribution was presumably due to low SNR of the acquired spin- and stimulated-echo signals, as is the larger variation of estimated parameters in the phantom experiments. The influence of SNR and partial volume was investigated with numerical phantom simulation and presented in the Supporting Information Figure S11. The voxelwise comparisons between the tissue parameters estimated by the proposed method and conventional method are shown in Supporting Information Figure S12.

Figure 8 demonstrates T_1 , T_2 , M_0 , α_{B1} , and ΔB_0 maps estimated by the proposed BUDA-MESMERISE

acquisition and unsupervised neural network-based estimation. Three out of the 24 slices covering whole brain are presented. It took 50 s to acquire the 24-slice data and 5.76 s to acquire 24-line calibration scan for coil sensitivity measurement. Whole-brain estimation results are shown in Supporting Information Figure S13. Although the effective TR was different for each acquisition and each slice, consistent estimation results were observed, indicating that the effect of varying effective TR was successfully captured through the signal model.

There are 2 factors that could affect the acquired signal when the echo-shifting is applied. One is crosstalk between slices, and the other is a magnetization transfer effect. To address the first issue, we used the slice-interleaving technique for which adjacent slices were not consecutively excited to reduce the crosstalk. Because we used short 90° RF pulses and slice interleaving, we

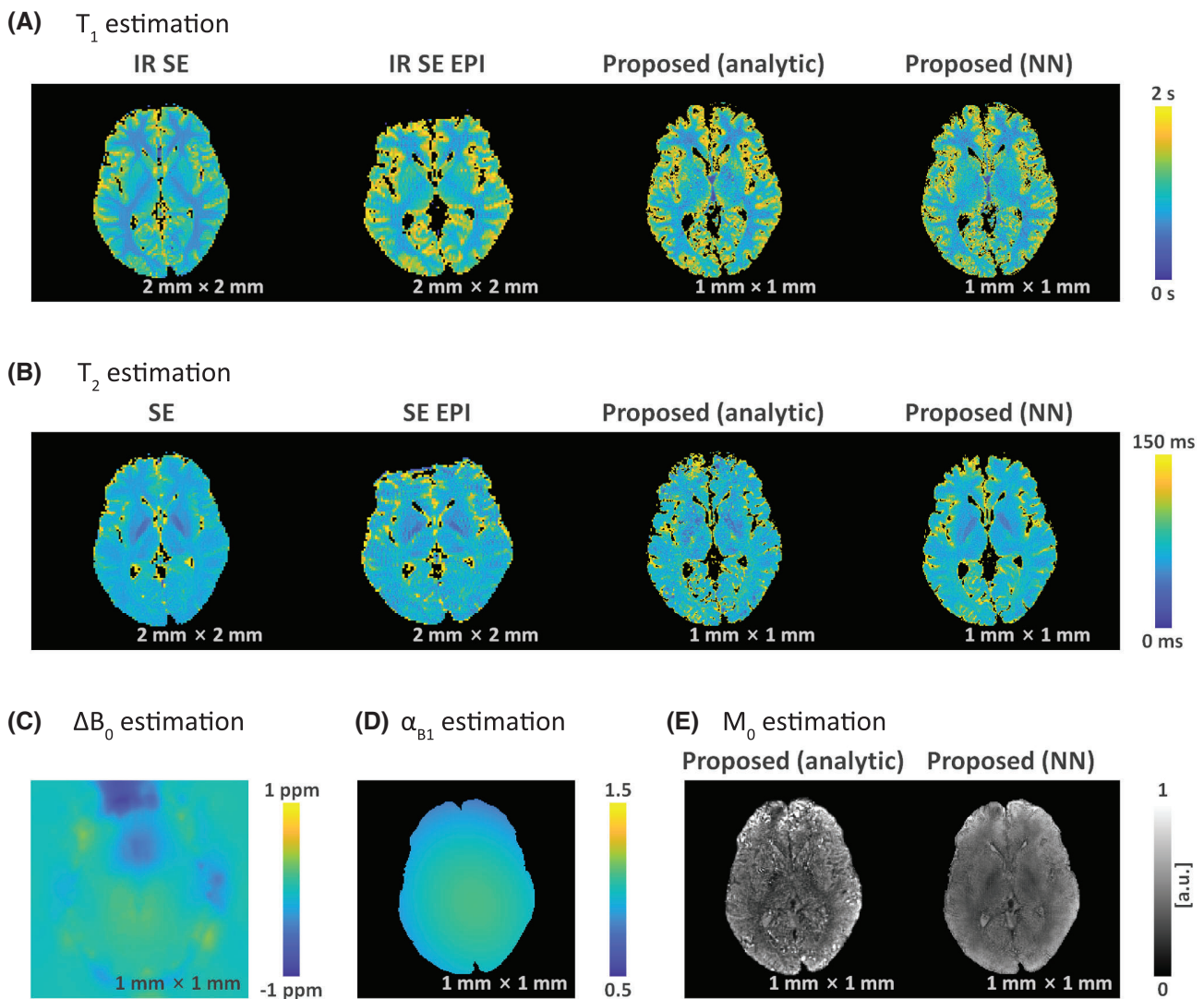


FIGURE 6 In vivo experiment results. Qualitative comparison of the proposed method with conventional methods. (A) T_1 estimation results. (B) T_2 estimation results. (C–E) ΔB_0 , α_{B1} , and M_0 estimation results from the proposed method, respectively

anticipated the magnetization transfer effects to be minor. In order to ascertain that the echo-shifting did not affect the signal from the different slice, we compared the stimulated-echo signals with different echo-shift factor. As shown in Supporting Information Figure S14(A), there is no noticeable signal difference between the acquired signal with and without echo-shifting, which shows that the crosstalk is insignificant on account of slice interleaving. In in vivo experiments, as shown in Supporting Information Figure S14(B), signal changes due to inconsistent ghost correction and CSF flow were observable; however, changes due to magnetization transfer were not identified. In terms of the estimated parameters, the single-slice experiment and the multislice experiment produce consistent results as shown in Supporting information Figure S15. This indicates that the echo-shifting can accelerate the acquisition speed without influencing

the other slices, as also shown earlier.³⁴ Incidentally, the ghost correction should be performed more precisely for the time-multiplexed acquisition because the eddy current effect increases as the duty cycle of gradient increases.

When the 3-pulse STEAM sequence was used for diffusion acquisition, stimulated echo can provide diffusion contrast with a high b value. This is because, during the mixing time, diffusion weighting continues with slow T_1 attenuation rather than fast T_2 decay. Although there was no diffusion gradient in the proposed parameter estimation, butterfly gradient (i.e., crusher and slice selection gradients) could inadvertently act as a diffusion gradient.⁵⁹ The butterfly gradient having an effect on the stimulated echo is shown in Supporting Information Figure S16. In order to verify the diffusion effect in our tissue parameter estimation, b value with respect to the TM and measured

(A) Phantom

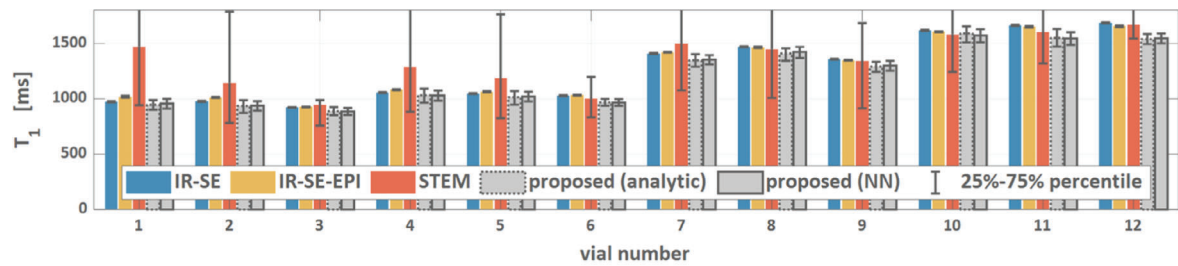
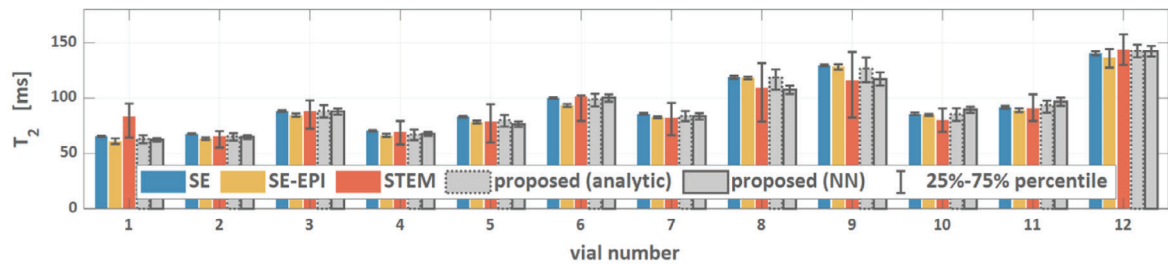
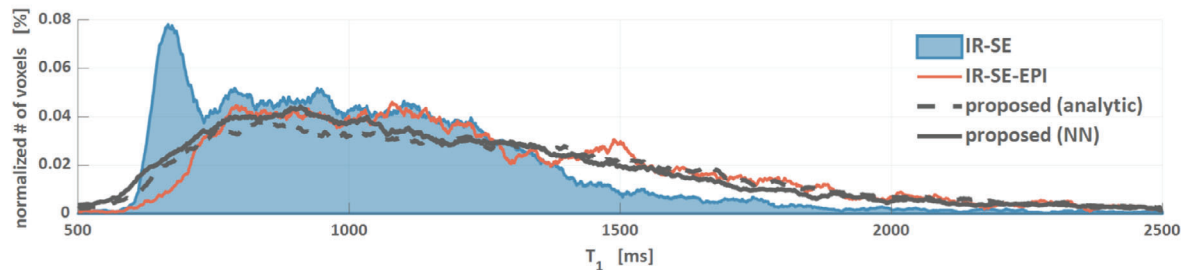
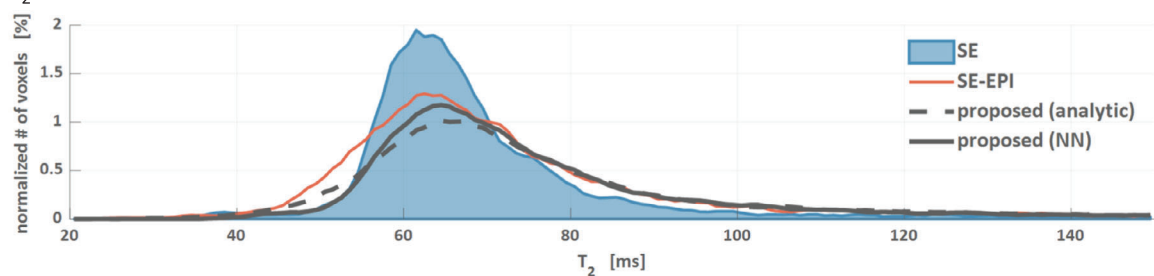
a T_1 estimationb T_2 estimation(B) *In vivo*a T_1 estimationb T_2 estimation

FIGURE 7 Quantitative comparison of the proposed method with conventional methods. (A) Phantom experiment results. (a) T_1 estimation results. (b) T_2 estimation results. The mean values of T_1 and T_2 in each vial are expressed as bar graph, and 25%–75% percentile as error bar. (B) *In vivo* experiment results. (a) T_1 estimation results. (b) T_2 estimation results

T_1 considering diffusion attenuation were calculated. An apparent diffusion coefficient of $10^{-3} \text{ mm}^2/\text{s}$ was assumed. The maximum b value in our experimental condition was smaller than 30 s/mm^2 , and the error of T_1 estimation was less than 5% when T_1 was smaller than 2000 ms.

5 | DISCUSSION AND CONCLUSION

In this study, a highly efficient MR parameter estimation framework was proposed. The proposed BUDA-MESMERISE acquisition/reconstruction enables

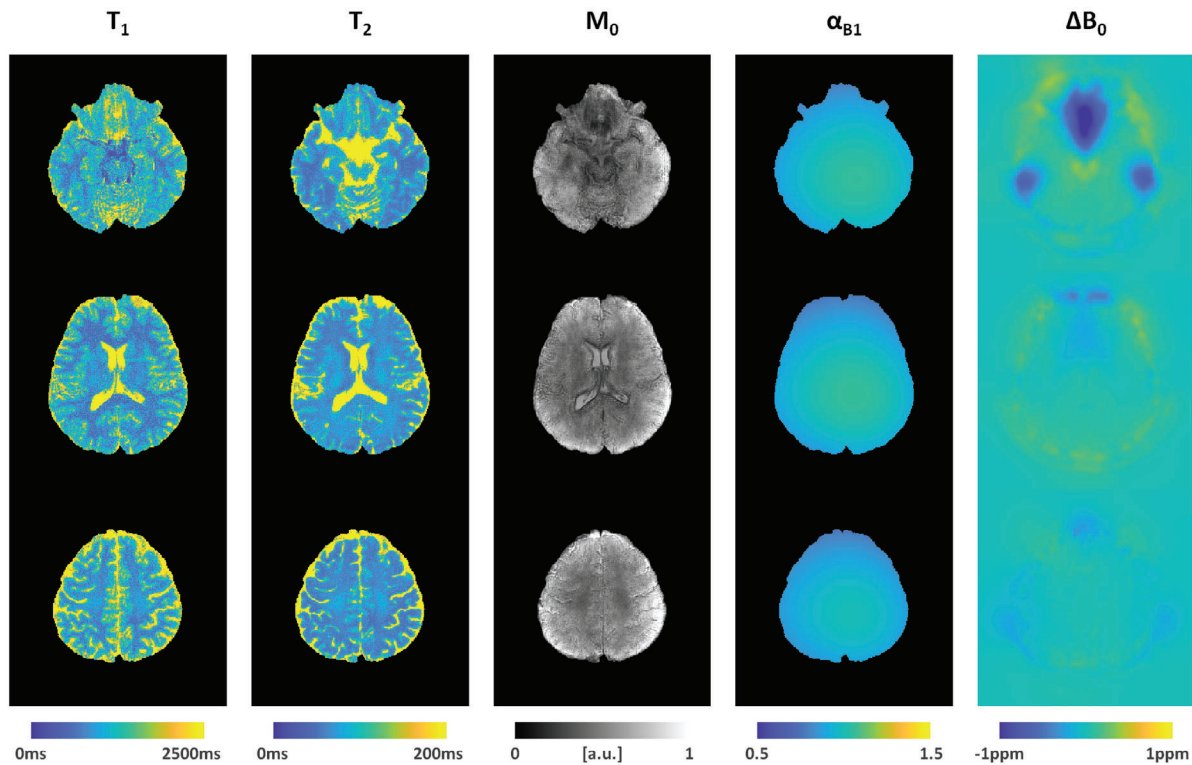


FIGURE 8 In vivo brain T_1 , T_2 , M_0 , α_{B1} , and ΔB_0 maps estimated by the proposed method with unsupervised neural network-based estimation. Three-slice results out of the 24 slices covering whole brain are presented

rapid acquisition of spin- and stimulated-echo signals to estimate distortion-corrected, coregistered T_1 , T_2 , M_0 , B_0 , and B_1 maps. With the STEAM EPI sequence consisting of three 90° RF pulses, spin- and stimulated-echo signals are acquired in rapid succession. These signals are generated from different pathways; thus, they possess distinct information on T_1 decay and α_{B1} modulation, as well as shared information on T_2 decay, TR_{eff} modulated M_0 , and ΔB_0 . This allows the estimation of T_1 , T_2 , M_0 , and α_{B1} maps. The concurrent acquisition and simultaneously varying imaging parameters of TE and TM enable coregistered parameter estimation. For rapid data acquisition, EPI readout is used for the spin- and stimulated-echo signals. We utilized BUDA for eliminating geometric distortion in EPI acquisition. BUDA augments the parallel imaging forward model with the B_0 inhomogeneity map estimated from the opposite phase-encoded acquisitions and incorporates structured low rank constraint into the reconstruction to gain robustness to potential shot-to-shot phase variation. In addition, the interleaved k-space sampling pattern between the opposite phase-encoded acquisitions enables higher in-plane acceleration, which reduces TE and T_2^* blurring.

For multislice imaging, echo-shifting and interleaved acquisition are applied to utilize the dead time between

the second and third RF pulses. The time multiplexed acquisition enables time-efficient data acquisition for multislice imaging. Because the STEAM sequence only utilizes 90° RF pulses and single-shot EPI acquisition is used, duty cycle can be increased with less concern about SAR. In order to estimate the parameter maps from the spin- and stimulated-echo signals, the analytic fitting and the unsupervised parameter estimation with a deep neural network were introduced. Both methods successfully estimated parameter maps of T_1 , T_2 , M_0 , and α_{B1} . The results obtained by the analytic fitting and the deep neural network were similar for all parameters, but the latter was more robust to noise than the analytic fitting. With a relatively short TR, signal intensity was affected by the effective TR; hence, this was considered for parameter estimation. In both phantom and in vivo brain experiments, the T_1 and T_2 estimation results showed agreement with conventional methods.

The advantages of the proposed method compared to other multiparametric quantitative MR techniques are rapid acquisition and yielding rich parameters. The proposed method simultaneously extracts the tissue parameters of T_1 , T_2 , and M_0 and the imaging conditions of ΔB_0 and α_{B1} . The time-efficient acquisition of the proposed method enables 50 s acquisition of $1 \times 1 \times 5 \text{ mm}^3$


resolution parameter maps. In addition, the proposed BUDA-MESMERISED could lend itself well to be translated to ultrahigh field because the influence of the ΔB_0 and α_{B1} can be eliminated from the parametric maps. A drawback of the proposed method using three 90° RF pulses is the reduced SNR compared to the conventional spin echo-based methods. The proposed deep neural network-based parameter estimation helps improve noise robustness by utilizing convolutional spatial priors. In addition, SNR per unit time is compensated by effective utilization of both spin- and stimulated-echo signals and the increased acceleration from echo-shifting.


To provide further quantitative information, an additional gradient-echo acquisition can be introduced after the first RF pulse. With this gradient echo signal, $T2^*$ could be estimated. For the neural network estimation, it is expected that the parameter estimation would become more efficient with a convergence condition rather than a fixed number of epochs. In addition, the MR physics-based network could be pretrained with training dataset and then refined by the new subject data, which is expected to reduce the computation time for parameter estimation. And estimation of the field inhomogeneity and distortion correction that were accomplished by FSL and BUDA reconstruction in this paper could be performed by the unsupervised model-based neural network as the proposed parameter estimation. The distortion correction with the model-based neural network is expected to expedite the correction process, especially for high-resolution data.

ACKNOWLEDGMENT

This research was supported by the following: Korea Health Industry Development Institute (KHIDI) funded by the Ministry of Health & Welfare, Republic of Korea (grant HI14C1135); the Korea Medical Device Development Fund (grant 202011B35); the MIT-Korea - KAIST Seed Fund of the MIT International Science and Technology Initiatives (MISTI); the Korea Institute of Science and Technology (grant 2E30971); the National Institutes of Health (NIH) (grants P41-EB030006, U01-EB026996, U01-EB025162, R01-EB028797, R03-EB031175, and R01MH111444); the Dutch Science Foundation (NWO) VIDI (grants 016-178-052 and 14637); the European Research Council (ERC) (grants 885876 and 639938); the German Research Foundation (DFG) (grants MO 2397/5-1, MO 2249/3-1, and MO 2397/4-1); the German Federal Ministry of Education and Research (BMBF) (grants 01EW1711A and B); and the Forschungszentren Medizintechnik Hamburg (FMTHH) (grant 01fmthh2017).

ORCID

Hyun Wook Park  <https://orcid.org/0000-0002-4757-1922>

Benedikt A. Poser  <https://orcid.org/0000-0001-8190-4367>

Berkin Bilgic  <https://orcid.org/0000-0002-9080-7865>

REFERENCES

1. Komiyama M, Yagura H, Baba M, et al. MR imaging: possibility of tissue characterization of brain tumors using T1 and T2 values. *Am J Neuroradiol*. 1987;8:65-70.
2. Just M, Thelen M. Tissue characterization with T1, T2, and proton density values: results in 160 patients with brain tumors. *Radiology*. 1988;169:779-785.
3. Larsson HBW, Frederiksen J, Petersen J, et al. Assessment of demyelination, edema, and gliosis by in vivo determination of T1 and T2 in the brain of patients with acute attack of multiple sclerosis. *Magn Reson Med*. 1989;11:337-348.
4. Jackson GD, Connelly A, Duncan JS, Grünwald RA, Gadian DG. Detection of hippocampal pathology in intractable partial epilepsy: increased sensitivity with quantitative magnetic resonance T2 relaxometry. *Neurology*. 1993;43:1793-1793.
5. Vymazal J, Righini A, Brooks RA, et al. T1 and T2 in the brain of healthy subjects, patients with Parkinson disease, and patients with multiple system atrophy: relation to iron content. *Radiology*. 1999;211:489-495.
6. Neema M, Goldberg-Zimring D, Guss ZD, et al. 3 T MRI relaxometry detects T2 prolongation in the cerebral normal-appearing white matter in multiple sclerosis. *Neuroimage*. 2009;46:633-641.
7. Shen Q, Du F, Huang S, Duong TQ. Spatiotemporal characteristics of postischemic hyperperfusion with respect to changes in T1, T2, diffusion, angiography, and blood-brain barrier permeability. *J Cereb Blood Flow Metab*. 2011;31:2076-2085.
8. Hamlin SA, Henry TS, Little BP, Lerakis S, Stillman AE. Mapping the future of cardiac MR imaging: case-based review of T1 and T2 mapping techniques. *Radiographics*. 2014;34:1594-1611.
9. Puntmann VO, Isted A, Hinojar R, Foote L, Carr-White G, Nagel E. T1 and T2 mapping in recognition of early cardiac involvement in systemic sarcoidosis. *Radiology*. 2017;285:63-72.
10. Caspar T, El Ghannudi S, Ohana M, et al. Magnetic resonance evaluation of cardiac thrombi and masses by T1 and T2 mapping: an observational study. *Int J Cardiovasc Imaging*. 2017;33:551-559.
11. Arcari L, Hinojar R, Engel J, et al. Native T1 and T2 provide distinctive signatures in hypertrophic cardiac conditions—comparison of uremic, hypertensive and hypertrophic cardiomyopathy. *Int J Cardiol*. 2020;306:102-108.
12. Huang Y, Majumdar S, Genant HK, et al. Quantitative MR relaxometry study of muscle composition and function in Duchenne muscular dystrophy. *J Magn Reson Imaging*. 1994;4:59-64.
13. Mwale F, Iatridis JC, Antoniou J. Quantitative MRI as a diagnostic tool of intervertebral disc matrix composition and integrity. *Eur Spine J*. 2008;17:432-440.
14. Matsubara S, Kawahara N, Horie A, et al. Magnetic resonance relaxometry improves the accuracy of conventional MRI in the diagnosis of endometriosis-associated ovarian cancer: a case report. *Molecular and Clinical Oncology*. 2019;11:296-300.

15. Schieda N, Lim CS, Zabihollahy F, et al. Quantitative prostate MRI. *J Magn Reson Imaging*. 2021;53:1632-1645.
16. Keenan KE, Biller JR, Delfino JG, et al. Recommendations towards standards for quantitative MRI (qMRI) and outstanding needs. *J Magn Reson Imaging: JMRI*. 2019;49:e26-e39.
17. Kingsley PB. Methods of measuring spin-lattice (T1) relaxation times: an annotated bibliography. *Concepts Magn Reson*. 1999;11:243-276.
18. Bydder GM, Young IR. MR imaging: clinical use of the inversion recovery sequence. *J Comput Assist Tomogr*. 1985;9:659-675.
19. Hahn EL. Spin echoes. *Phys Rev*. 1950;80:580.
20. Henoumont C, Laurent S, Vander EL. How to perform accurate and reliable measurements of longitudinal and transverse relaxation times of MRI contrast media in aqueous solutions. *Contrast Media Mol Imaging*. 2009;4:312-321.
21. Meiboom S, Gill D. Modified spin-echo method for measuring nuclear relaxation times. *Review of Scientific Instruments*. 1958;29:688-691.
22. Ben-Eliezer N, Sodickson DK, Block KT. Rapid and accurate T2 mapping from multi-spin-echo data using Bloch-simulation-based reconstruction. *Magn Reson Med*. 2015;73:809-817.
23. Welsch GH, Scheffler K, Mamisch TC, et al. Rapid estimation of cartilage T2 based on double echo at steady state (DESS) with 3 Tesla. *Magn Reson Med*. 2009;62:544-549.
24. Heule R, Ganter C, Bieri O. Triple echo steady-state (TESS) relaxometry. *Magn Reson Med*. 2014;71:230-237.
25. Gras V, Farrher E, Grinberg F, Shah NJ. Diffusion-weighted DESS protocol optimization for simultaneous mapping of the mean diffusivity, proton density and relaxation times at 3 Tesla. *Magn Reson Med*. 2017;78:130-141.
26. Schmitt P, Griswold MA, Jakob PM, et al. Inversion recovery TrueFISP: quantification of T1, T2, and spin density. *Magn Reson Med*. 2004;51:661-667.
27. Ma D, Gulani V, Seiberlich N, et al. Magnetic resonance fingerprinting. *Nature*. 2013;495:187-192.
28. Sbrizzi A, van der Heide O, Cloos M, et al. Fast quantitative MRI as a nonlinear tomography problem. *Magn Reson Imaging*. 2018;46:56-63.
29. Warntjes JBM, Dahlqvist O, Lundberg P. Novel method for rapid, simultaneous T1, T2, and proton density quantification. *Magn Reson Med*. 2007;57:528-537.
30. Leroi L, Gras V, Boulant N, et al. Simultaneous proton density, T1, T2, and flip-angle mapping of the brain at 7 T using multiparametric 3D SSFP imaging and parallel-transmission universal pulses. *Magn Reson Med*. 2020;84:3286-3299.
31. Börnert P, Jensen D. Single-shot-double-echo EPI. *Magn Reson Imaging*. 1994;12:1033-1038.
32. Shi X, Kim SE, Jeong EK. Single-shot T1 mapping using simultaneous acquisitions of spin-and stimulated-echo-planar imaging (2D ss-SESTEPI). *Magn Reson Med*. 2010;64:734-742.
33. Zhang Y, Wells SA, Hernando D. Stimulated echo based mapping (STEM) of T1, T2, and apparent diffusion coefficient: validation and protocol optimization. *Magn Reson Med*. 2019;81:167-181.
34. Fritz FJ, Poser BA, Roebroek A. MESMERISED: super-accelerating T1 relaxometry and diffusion MRI with STEAM at 7 T for quantitative multi-contrast and diffusion imaging. *Neuroimage*. 2021;239:118285.
35. Doneva M, Börnert P, Eggers H, Stehning C, SÉNÉgas J, Mertins A. Compressed sensing reconstruction for magnetic resonance parameter mapping. *Magn Reson Med*. 2010;64:1114-1120.
36. Zhang T, Pauly JM, Levesque IR. Accelerating parameter mapping with a locally low rank constraint. *Magn Reson Med*. 2015;73:655-661.
37. Cohen O, Zhu B, Rosen MS. MR fingerprinting deep reconstruction network (DRONE). *Magn Reson Imaging*. 2018;80:885-894.
38. Cai C, Wang C, Zeng Y, et al. Single-shot T2 mapping using overlapping-echo detachment planar imaging and a deep convolutional neural network. *Magn Reson Imaging*. 2018;80:2202-2214.
39. Fang Z, Chen Y, Liu M, et al. Deep learning for fast and spatially constrained tissue quantification from highly accelerated data in magnetic resonance fingerprinting. *IEEE Trans Med Imaging*. 2019;38:2364-2374.
40. Liu F, Feng L, Kijowski R. MANTIS: model-augmented neural network with incoherent k-space sampling for efficient MR parameter mapping. *Magn Reson Imaging*. 2019;82:174-188.
41. Liu F, Kijowski R, Feng L, El Fakhri G. High-performance rapid MR parameter mapping using model-based deep adversarial learning. *Magn Reson Imaging*. 2020;74:152-160.
42. Liao C, Cao X, Cho J, Zhang Z, Setsompop K, Bilgic B. Highly efficient MRI through multi-shot echo planar imaging. *Wavelets and Sparsity XVIII*. Vol 11138. International Society for Optics and Photonics; 2019.
43. Cao X, Liao C, Zhang Z, et al. Efficient T2 mapping with blip-up/down EPI and gSlider-SMS (T2-BUDA-gSlider). *Magn Reson Med*. 2021;86:2064-2075.
44. Andersson JL, Skare S, Ashburner J. How to correct susceptibility distortions in spin-echo echo-planar images: application to diffusion tensor imaging. *Neuroimage*. 2003;20:870-888.
45. Smith SM, Jenkinson M, Woolrich MW, et al. Advances in functional and structural MR image analysis and implementation as FSL. *Neuroimage*. 2004;23:S208-S219.
46. Samsonov AA, Kholmovski EG, Parker DL, Johnson CR. POCSENSE: POCS-based reconstruction for sensitivity encoded magnetic resonance imaging. *Magn Reson Med*. 2004;52:1397-1406.
47. Haldar JP. Low-rank modeling of local k-space neighborhoods (LORAKS) for constrained MRI. *IEEE Trans Med Imaging*. 2013;33:668-681.
48. Shin PJ, Larson PE, Ohliger MA, et al. Calibrationless parallel imaging reconstruction based on structured low-rank matrix completion. *Magn Reson Med*. 2014;72:959-970.
49. Jin KH, Lee D, Ye JC. A general framework for compressed sensing and parallel MRI using annihilating filter based low-rank Hankel matrix. *IEEE Transactions on Computational Imaging*. 2016;2:480-495.
50. Mani M, Jacob M, Kelley D, Magnotta V. Multi-shot sensitivity-encoded diffusion data recovery using structured low-rank matrix completion (MUSSELS). *Magn Reson Med*. 2017;78:494-507.
51. Uecker M, Lai P, Murphy MJ, et al. ESPIRiT—an eigenvalue approach to autocalibrating parallel MRI: where SENSE meets GRAPPA. *Magn Reson Med*. 2014;71:990-1001.
52. Moonen CTW, Liu G, Gelderen PV, Sobering G. A fast gradient-recalled MRI technique with increased sensitivity

to dynamic susceptibility effects. *Magn Reson Med*. 1992;26:184-189.

53. Liu G, Sobering G, Duyn J, Moonen CT. A functional MRI technique combining principles of echo-shifting with a train of observations (PRESTO). *Magn Reson Med*. 1993;30:764-768.
54. He K, Zhang X, Ren S, Sun J. Deep residual learning for image recognition. In Proceedings IEEE Conference on Computer Vision and Pattern Recognition (CVPR), 2016. P. 770-778.
55. Kingma DP, Ba J. Adam: A method for stochastic optimization. 2014. arXiv preprint: arXiv:1412.6980.
56. Hattori K, Ikemoto Y, Takao W, et al. Development of MRI phantom equivalent to human tissues for 3.0-T MRI. *Med Phys*. 2013;40:032303.
57. Setsompop K, Gagoski BA, Polimeni JR, Witzel T, Wedeen VJ, Wald LL. Blipped-controlled aliasing in parallel imaging for simultaneous multislice echo planar imaging with reduced g-factor penalty. *Magn Reson Med*. 2012;67:1210-1224.
58. O'Brien JS, Sampson EL. Lipid composition of the normal human brain: gray matter, white matter, and myelin. *J Lipid Res*. 1965;6:537-544.
59. Lundell H, Alexander DC, Dyrby TB. High angular resolution diffusion imaging with stimulated echoes: compensation and correction in experiment design and analysis. *NMR Biomed*. 2014;27:918-925.

SUPPORTING INFORMATION

Additional supporting information may be found in the online version of the article at the publisher's website.

Figure S1. The pulse sequence diagram of BUDA-MESMERISE. Gradients are presented in the merged form and those for slice selection and imaging that do not affect the signal formation and modulation are excluded.

Figure S2. The numerical phantom and the estimated parameter maps from the proposed neural network-based parameter estimation method.

Figure S3. The numerical phantom simulation with various noise levels. The tissue parameters were estimated with the proposed parameter estimation methods, the analytic fitting and the unsupervised parameter estimation with a deep neural network.

Figure S4. Time multiplexed acquisition scheme consisting of echo-shifting and interleaved acquisition (a), corresponding sequence timing (b) and effective TR (c) for whole-brain imaging.

Figure S5. Phantom experiment results. (Aa) Acquired blip-up/down image with in-plane acceleration factor of two. These aliased images show geometric distortion in opposite directions according to blip up and down. (Ab) POCSENSE reconstructed images of (Aa). (Ac) Distortion-corrected image with BUDA reconstruction. (B) Distortion-corrected spin echo images and stimulated echo images with five different [TE, TM] combinations.

Figure S6. Spin-echo images with TR = 30 s and TR = 2.5 s, and difference images.

Figure S7. In vivo brain experiment results. (Aa) Acquired blip-up/down image with in-plane acceleration factor of two. These aliased images show geometric distortion in opposite directions according to blip up and down. (Ab) POCSENSE reconstructed images of (Aa). (Ac) Distortion-corrected image with BUDA reconstruction. (B) Distortion-corrected spin echo images and stimulated echo images with five different [TE, TM] combinations.

Figure S8. The numerical phantom simulation with an imperfect slice profile.

Figure S9. In vivo brain M_0 , ΔB_0 , and α_{B1} maps estimated by the proposed method and conventional methods.

Figure S10. Loss graph of the parameter estimation network according to the epoch and the parameter estimation results at five points.

Figure S11. Histogram of the estimated parameters of the numerical phantom with various noise levels.

Figure S12. Voxelwise comparison of the tissue parameters estimated by the proposed method and the reference method.

Figure S13. In vivo whole brain T_1 , T_2 , M_0 , α_{B1} and B_0 maps estimated by the proposed method and unsupervised neural network-based estimation method.

Figure S14. Stimulated-echo images of a brain phantom (A) and in vivo brain (B) with (a) and without (b) echo-shifting and the absolute signal difference (c). TR = 5 s, TE = 82 ms, TM = 1000 ms, in-plane acceleration = 2, FOV = 224 mm × 224 mm, slice thickness = 5 mm, resolution = 1 mm × 1 mm are used both for the phantom experiment and in vivo experiment.

Figure S15. In vivo brain T_1 , T_2 , M_0 , α_{B1} maps estimated by the experiment with and without echo-shifting and interleaved acquisition.

Figure S16. (a) RF pulse and gradients that can function as diffusion gradient. Gradient combination of crusher gradient and slice selection gradient, referred as butterfly gradient, which affects to the stimulated echo is colored. (b) Calculated b-value with respect to mixing time. (c) Estimated T_1 value considering diffusion attenuation with respect to true T_1 value.

Table S1. Imaging parameters for reference in vivo ΔB_0 and α_{B1} experiments

How to cite this article: So S, Park HW, Kim B, et al. BUDA-MESMERISE: Rapid acquisition and unsupervised parameter estimation for T_1 , T_2 , M_0 , B_0 , and B_1 maps. *Magn Reson Med*. 2022;88:292-308. doi: 10.1002/mrm.29228